Article

Study of the Cylinder Deactivation on Tribological Parameters and Emissions in an Internal Combustion Engine

Sofia Orjuela Abril [1,*], Marlen Del Socorro Fonseca-Vigoya [1] and Carlos Pardo García [2]

[1] Programa de Administración de Empresas, Universidad Francisco de Paula Santander, San José de Cúcuta 540001, Colombia; marlenfonseca@ufps.edu.co

[2] Programa de Ingeniería de Sistemas, Universidad Francisco de Paula Santander, San José de Cúcuta 540001, Colombia; carlospardo@ufps.edu.co

* Correspondence: sofiaorjuela@ufps.edu.co; Tel.: +57-7-5-776-655

Abstract: In the present investigation, a study is carried out using numerical simulation on the effects of cylinder deactivation on tribological parameters and emissions in an internal combustion engine. For the development of the research, a tribological model was used to predict the characteristics of the lubrication film, friction conditions, blow-by gas, and deformation of the piston rings. Additionally, the construction of a CFD model was carried out to describe the kinematic movement of the engine piston. The analysis of results allowed for the demonstration of the active cylinders presenting an increase of 21.53% and 7.65% in the pressure and temperature in the cylinder wall. Additionally, the active cylinders present a reduction of 11.33% in the minimum thickness of the lubrication film and an increase in the friction force due to asperities, which implies an increase of 33% in power losses due to friction. The implementation of technologies such as cylinder deactivation causes an increase in combustion gas leaks caused by the increase in pressure of the active cylinders. However, the use of this technology allows reducing 9.09%, 8.26%, and 7.41% in CO, HC, and NO emissions. Although the use of technologies such as cylinder deactivation allows significant fuel savings, it is necessary to consider the negative effects caused by this technology, such as the increase in combustion gas leaks and the increase in power loss by the greatest frictional forces.

Keywords: cylinder deactivation; power loss; piston compression ring; blow-by gas; emissions

1. Introduction

Due to today's stringent emission control regulations, manufacturers and researchers have focused efforts on minimizing fuel consumption, improving performance, and reducing greenhouse gas emissions caused by internal combustion engines (ICE) [1–3]. The above aims to mitigate the environmental impact and avoid the accelerated consumption of fossil fuel reserves. Research in the literature indicates that approximately 50–60% of the energy contained in fuel is lost due to thermal inefficiencies [4]. In addition, the friction between the internal components can produce losses between 4 and 20% depending on the load conditions of the engine [5,6]. Since 99.8% of the demand in the transport sector comes from hydrocarbon fueled engines, it is necessary to implement alternatives to reduce the sources of energy losses in engine components.

One of the main energy-loss sources in ICEs is the interaction between the piston rings and the cylinder liner. The main objective of the compression rings is to form a hermetic seal between the cylinder liner and the piston to mitigate the leakage of combustion gases. This makes it possible to avoid pressure loss inside the combustion chamber. However, this type of sealing contributes significantly to energy losses due to frictional conditions between the piston rings and the cylinder liner. Additionally, the flexibility and thinness of the compression ring affects the sealing ability of the chamber. The above conditions lead to an increase in harmful gases from the engine [7] due to the unburned fuel trapped

between the piston rings, promoting the formation of hydrocarbon emissions [8]. Studies indicate that between 3 and 5% of the total ICE losses are a consequence of the interaction between the piston ring and the cylinder liner [9]. In the case of combustion gas leaks, an energy loss of between 2 and 7% is attributed. Therefore, the dynamic behavior and the sealing capacity of the compression rings are aspects that can be intervened to achieve a significant improvement in the energy efficiency of the ICE [10].

Over the years, different strategies have been developed to increase the efficiency of ICEs. Among which are improvements in combustion systems, engine tribology, electronic control, and detection algorithms [11–14]. Additionally, technologies such as exhaust gas recirculation [15], turbocharging [16], direct injection, HCCI (homogeneous charge compression ignition) engines [17], alternative biofuels [18], ratios of variable compression [19–21], and cylinder deactivation (CDA) [21]. The latter has received high interest in its application for gasoline engines. Since cylinder deactivation allows for high emission reductions and energy savings [8].

The CDA consists of the deactivation of some cylinders, which causes the rest of the active cylinders to require a higher load condition to maintain the brake mean effective pressure (BMEP). This causes an increase in intake manifold pressure and a reduction in pumping losses in gasoline engines [22]. Studies indicate that the application of CDA can lead to a 17–25% reduction in brake specific fuel consumption (BSFC) [23]. This reduction is mainly attributed to the decrease in pumping losses.

Another of the main influencing factors in fuel consumption is the mechanical losses of the engine. Depending on the load condition, about 20% of the fuel energy is used to overcome mechanical actuation and friction [24]. After cylinder deactivation, pressure and temperature variables are factors that have a notorious impact on the viscosity and thickness of the lubricating oil. Bewsher et al. [25] indicated that total friction losses increased by 9.53% due to cylinder deactivation. Therefore, it is necessary to consider the influence of the CDA on the tribological characteristics of the engine. In general, the tribological behavior of the conjunction of the piston rings and the cylinder liner are key to reducing friction losses. Additionally, the dynamics of the ring body affects the leakage gases and the distribution of oil in the piston ring pack [26].

The investigations described previously show the importance of the tribological conditions at the conjunction of the piston rings and the cylinder liner on power losses and engine emissions. Due to the above, this research aims to evaluate the effect of technologies such as cylinder deactivation on the tribological characteristics of a compression ignition engine. The study consists of evaluating the conditions of the combustion chamber, analyzing the friction force, loss power, combustion gas leakage, and CO, HC, and NO emissions.

2. Numerical Model

2.1. Tribological Model

To determine the hydrodynamic pressure between the conjunction of the piston rings and the cylinder liner, the modification of the Reynolds equation proposed by Guo et al. [27] was used, as described in Equation (1).

$$\frac{\partial}{\partial x}\left(\phi_x \frac{h^3}{\eta}\frac{\partial P}{\partial x}\right) + \frac{\partial}{\partial y}\left(\phi_y \frac{h^3}{\eta}\frac{\partial P}{\partial y}\right) = 6v_p\left(\phi_c \frac{\partial h}{\partial y} + \sigma \frac{\partial \phi_s}{\partial y}\right) + 12\phi_c \frac{\partial h}{\partial t} \tag{1}$$

where η is the viscosity of the lubricant, h is the thickness of the lubricant, P is the film pressure of the lubricating oil, v_p is the piston velocity, ϕ_x and ϕ_y are the pressure flow factors, σ is the composite roughness, ϕ_c is a contact factor, and ϕ_s is the shear flow factor. The pressure flow factors (ϕ_x, ϕ_y) were calculated using Equation (2) [28].

$$\phi_x = \phi_y = 1 - 0.9e^{-0.56(h/\sigma)} \tag{2}$$

Since the conditions of pressure and temperature affect the properties of the oil, the relationship proposed by Dowson and Higginson was used to determine the density of the lubricating oil, as shown in Equation (3) [29].

$$\rho = \left[\rho_o + \frac{6 \times 10^{-10}(P - P_o)\rho_o}{1 + 1.7 \times 10^{-9}(P - P_o)} + 1 \right] [1 - \beta(T - T_o)] \tag{3}$$

The subscript o refers to environmental conditions, and β is the coefficient of thermal expansion.

In the case of the viscosity of the lubricating oil, the model proposed by Houpert was used, which is described in Equation (4) [30].

$$\eta = \eta_o \left\{ (\ln \eta_o + 9.67) \left[\left(\frac{T - 138}{T_o - 138} \right)^{-S_o} \left(1 + \frac{P - P_o}{1.98 \times 10^8} \right)^Z - 1 \right] \right\} \tag{4}$$

where Z is the lubricant piezo-viscosity index and S_o is the thermo-viscosity index, respectively. The Z and S_o indices were determined by Equations (5) and (6).

$$Z = \alpha_o c_p / \ln\left(\frac{\eta_o}{\eta_\infty} \right) \tag{5}$$

$$S_o = \beta_o / \ln\left(\frac{\eta_o}{\eta_\infty} \right) \tag{6}$$

where β_o is the thermo-viscosity coefficient and α_o is the atmospheric piezo-viscosity coefficient, respectively. c_p and η_∞ are model constants, which were calculated using Equations (7) and (8).

$$c_p = 1.98 \times 10^8 \text{ Pa} \tag{7}$$

$$\eta_\infty = 6.31 \times 10^{-5} \text{ Pa·s} \tag{8}$$

The thickness of the lubricating oil film was calculated by means of Equation (9).

$$h = h_m + h_p \tag{9}$$

where h_m is the minimum oil film thickness and h_p is the thickness of the oil due to the geometric profile of the piston ring, respectively. For the calculation of h_p Equation (10) was used [31].

$$h_p = \frac{4\delta_o}{b^2} y^2 \tag{10}$$

where b is the piston ring axial width and δ_o is the crown height, respectively.

2.2. Friction Force Model

The conjunction of the piston ring and the cylinder liner cause the presence of two types of friction forces, which are a consequence of the viscosity of the lubrication film and the interaction between the asperities present on the surface of the piston rings and the cylinder liner. To determine the viscous friction force (f_v), Equation (11) was used.

$$f_v = \tau_{ss} \times (A - A_e) \tag{11}$$

where τ_{ss} is the viscous shear stress, A_e is the real area of contact area and A is the apparent contact area, respectively. To determine τ_{ss} Equation (12) was used [32].

$$\tau_{ss} = \left| \vec{v}_p \frac{\eta}{h} \pm \vec{\nabla} P \frac{h}{2} \right| \tag{12}$$

The real contact area (A_e) was calculated by means of the Equation (13).

$$A_e = A F_{2(\lambda)} (\pi \zeta \kappa \sigma)^2 \tag{13}$$

where ξ is the asperity distribution per unit contact area, κ is the average asperity tip radius of curvature, and $F_{2(\lambda)}$ is the statistical function of the Stribeck lubricant film ratio (λ). The statistical function $F_{2(\lambda)}$ was determined by Equation (14) [33].

$$F_{2(\lambda)} = \left\{ \begin{array}{c} -0.0018\lambda^5 + 0.0281\lambda^4 - 0.1728\lambda^3 + 0.5258\lambda^2 - 0.8043\lambda + 0.5003\ \lambda \leq 2.295 \\ 0 \quad \lambda > 2.295 \end{array} \right\} \tag{14}$$

In the case of the asperity friction force (f_a), this was calculated by means of the Equation (15) [34].

$$f_a = E_{ss}A_e + \zeta W_a \tag{15}$$

where E_{ss} is the limiting Eyring shear stress, ζ is the coefficient of asperity shear strength, and W_a is the asperity contact load. To determine the asperity contact load (W_a), the model proposed by Greenwood and Tripp was used, as shown in Equation (16) [34].

$$W_a = \frac{16\sqrt{2}\pi}{15} A F_{5/2(\lambda)} E'(\xi\kappa\sigma)^2 \left(\frac{\sigma}{\kappa}\right)^{1/2} \tag{16}$$

The equivalent Young's modulus of elasticity (E') was calculated from the Equation (17).

$$\frac{1}{E'} = \frac{1 - v_c^2}{E_c} + \frac{1 - v_p^2}{E_p} \tag{17}$$

where E_c and E_p are the modulus of elasticity of the cylinder liner and piston ring, respectively. v_c and v_p are the Poisson's ratio of the cylinder liner and piston ring, respectively. $F_{5/2(\lambda)}$ is a statistical function of lubricant film ratio approximated by a fifth order polynomial as [35]:

$$F_{5/2(\lambda)} = \left\{ \begin{array}{c} -0.0046\lambda^5 + 0.0574\lambda^4 - 0.2958\lambda^3 + 0.7844\lambda^2 - 1.0776\lambda + 0.6167\ \ \lambda \leq 2.224 \\ 0 \quad \lambda > 2.224 \end{array} \right\} \tag{18}$$

2.3. Gas Blow-by Model

The mass flow of combustion gases through the piston rings was calculated assuming an isentropic flow condition through an equivalent orifice, as shown in Equation (19) [36].

$$\dot{m}_f = \frac{f_m C_d A_g P_u}{(RT_u)^{1/2}} \tag{19}$$

where C_d is the coefficient of discharge, T_u is the orifice upstream temperature, f_m is the compressibility factor, A_g is the ring end-gap area, and R is the gas constant, respectively. The compressibility factor (f_m) was calculated from Equation (20) [36].

$$f_m = \left\{ \begin{array}{c} \sqrt{\gamma_s}\left(\frac{2}{\gamma_s+1}\right)^{\frac{\gamma_s+1}{2\gamma_s-2}},\ \ \frac{p_d}{p_u} > \left(\frac{2}{\gamma_s+1}\right)^{\frac{\gamma_s}{\gamma_s-1}} \\ C_d,\ \ \frac{p_d}{p_u} \leq \left(\frac{2}{\gamma_s+1}\right)^{\frac{\gamma_s}{\gamma_s-1}} \end{array} \right\} \tag{20}$$

where p_d and p_u are the downstream pressure and upstream pressure, respectively. C_d is the discharge coefficient, calculated from Equation (21).

$$C_d = 0.85 - 0.25\left(\frac{p_d}{p_u}\right)^2 \tag{21}$$

2.4. Deformation Model

The equations used to describe the deformation of the piston rings are given below:

$$\rho_p A_p \frac{\partial^2}{\partial t^2}(u) - f_r = -\frac{E_p I_p}{R_p^4}\left[\frac{\partial^3}{\partial \theta^3}(\omega) + \frac{\partial^4}{\partial \theta^4}(u)\right] + \frac{E_p A_p}{R_p^2}\left[-u + \frac{\partial}{\partial \theta}(\omega)\right] \qquad (22)$$

$$\rho_p A_p \frac{\partial^2}{\partial t^2}(\omega) - f_t = \frac{E_p I_p}{R_p^4}\left[\frac{\partial^2}{\partial \theta^2}(\omega) + \frac{\partial^3}{\partial \theta^3}(u)\right] + \frac{E_p A_p}{R_p^2}\left[-\frac{\partial}{\partial \theta}(u) + \frac{\partial^2}{\partial \theta^2}(\omega)\right] \qquad (23)$$

where ρ_p is the piston ring material density, A_p is the cross-sectional area of the ring, I_p is the second area moment of inertia, R_p is the ring radius of curvature, and θ is the angular position along the ring circumference, f_r and f_t are the radial force and tangential force acting on the piston ring, respectively.

3. Numerical Procedure

To predict the kinematic movement and the load conditions of the piston, a CFD model of the engine geometry was made, as shown in Figure 1. Numerical simulations were carried out using the free software OpenFOAM®. The geometric characteristics of the engine are shown in Table 1.
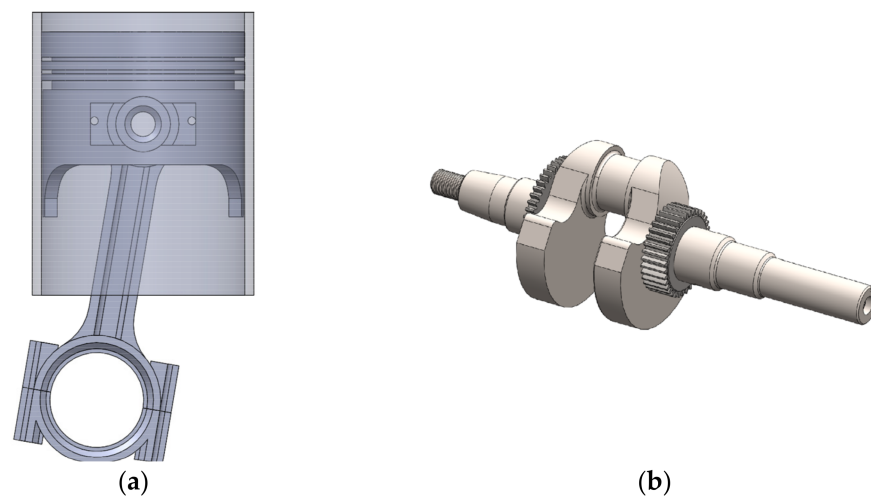

| (a) | (b) |

Figure 1. Internal combustion engine geometry (**a**) piston-connecting rod and (**b**) crankshaft.

Table 1. Geometric characteristics of the engine.

Parameter	Value	Unit
Piston radius	39	mm
Piston area	4778.36	mm^2
Piston mass	0.305	kg
Crankshaft radius	48	mm
Length of piston skirt	48	mm
Stroke	104.9	mm
Length of connecting rod	106	mm

For the numerical simulation, a computational domain formed by the surface of the cylinder liner, the surface of the piston rings, and the piston skirt was established. The CFD model also involves part of the engine crankcase and combustion chamber to describe the piston's entire movement during the combustion cycle. For the development of the research, a torque condition of 250 Nm and a rotation speed of 2000 rpm in the engine were used as a reference.

The Navier–Stokes's equations were used to govern the behavior of the numerical simulation. The mesh of the geometry was built using the SALOME software. The convergence was defined in a residual value of 10^{-4}, 10^{-7}, and 10^{-4} in the dissipation rate, energy, and turbulence kinetic energy, respectively [37]. The properties of the lubricating oil between the cylinder liner and the piston rings are described in Table 2, the characteristics of which are based on the SAE 10W40 lubricant.

Table 2. Lubricating oil properties.

Properties	Unit	SAE 10W40
Kinematic viscosity (40 °C)	m^2/s	91.057×10^{-6}
Dynamic viscosity (40 °C)	m^2/s	105.10×10^{-6}
Density (40 °C)	kg/m^3	866
Pressure—viscosity coefficient	m^2/N	1×10^{-8}
Flash point	°C	230

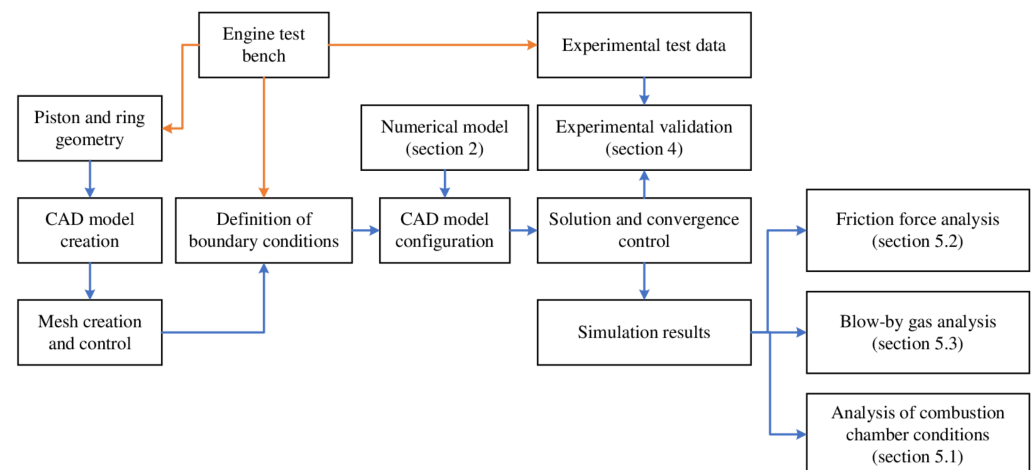The general methodology used for this research is described in Figure 2.

Figure 2. Research methodology.

From the reference engine, the geometric characteristics of the piston, crankshaft, and connecting rod for the CFD model were obtained. Additionally, data from the experimental tests were collected to define the boundary conditions of the numerical simulation, such as flow, temperature, and pressure. For the initial condition of the lubrication film between the cylinder liner and the piston rings, a distribution of 10% oil and 90% air was established, respectively.

4. Experimental Validation

To verify the prediction capacity of the numerical model, a comparison was made with the friction force on the cylinder liner, obtained through experimental tests. The friction force measurement was carried out using a strain gauge sensor to calculate the deformation in the cylinder liner. The characteristics of the sensor are shown in Table 3.

Table 3. Characteristics of the strain gauge sensor.

Parameter	Value	Unit
Maximum operating temperature	1150	°C
Overall length	6.30	mm
Gauge resistance	120	Ω
Gage length	2.54	mm
Grid width	4.55	mm

The determination of the experimental friction force (F_e) was carried out using Equations (24) and (25) [38].

$$\frac{V_1}{V_2} = -\frac{\varepsilon \cdot G_f}{4 + 2\varepsilon \cdot G_f} \tag{24}$$

$$F_e = \varepsilon \cdot E_c \cdot A_s \tag{25}$$

where V is the voltage, A_s is the area of the strain gauge sensor, G_f is the calibration factor of the strain gage $\left(G_f = 2\right)$, and ε is the longitudinal unit strain of the sensor. The experimental setup for friction force signal processing is indicated in Figure 3.
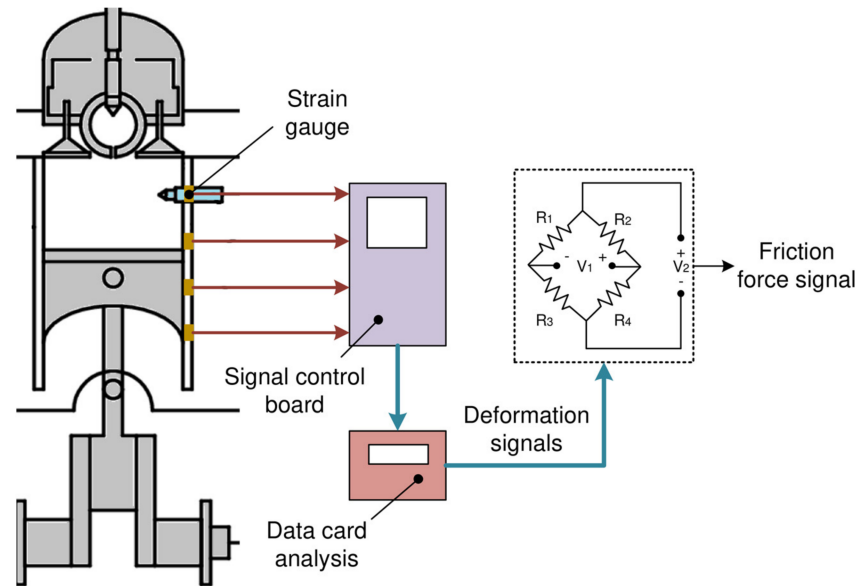
Figure 3. Measurement process of the friction force signal.

Figure 4 shows the comparison of the friction force between the experimental results and the numerical simulation for different crank angle positions.
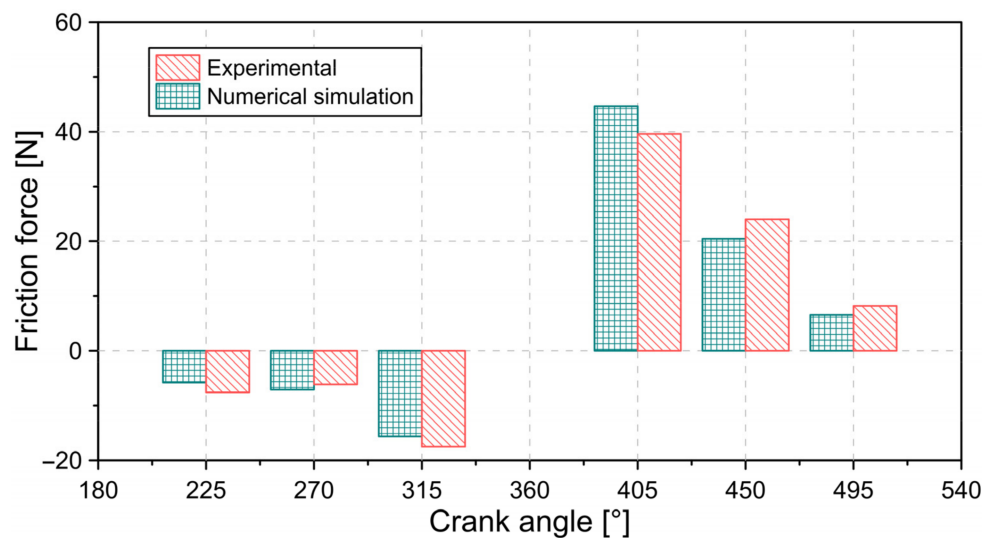

Figure 4. Friction force obtained from numerical simulation and experimental tests.

From the comparison shown in Figure 4, it is possible to demonstrate an adequate concordance between the predictions of the numerical model and the results obtained from the experimental tests. On average, a relative error of 16% was obtained with a maximum

error of 23%, which is in agreement with the investigations reported in the literature [39,40]. Deviations from numerical predictions can be a consequence of several variables, such as pressure change in the combustion chamber, lubrication film irregularities, and changes in lubricant properties.

5. Results and Discussion

5.1. Analysis of Combustion Chamber Conditions

During the cylinder deactivation process, two cylinders are active, and two cylinders are deactivated. Under standard operating conditions, all four engine cylinders remain operational. Figure 5 shows the behavior of the pressure in the active cylinder chamber, the deactivated cylinder, and the cylinder under normal engine operating conditions.
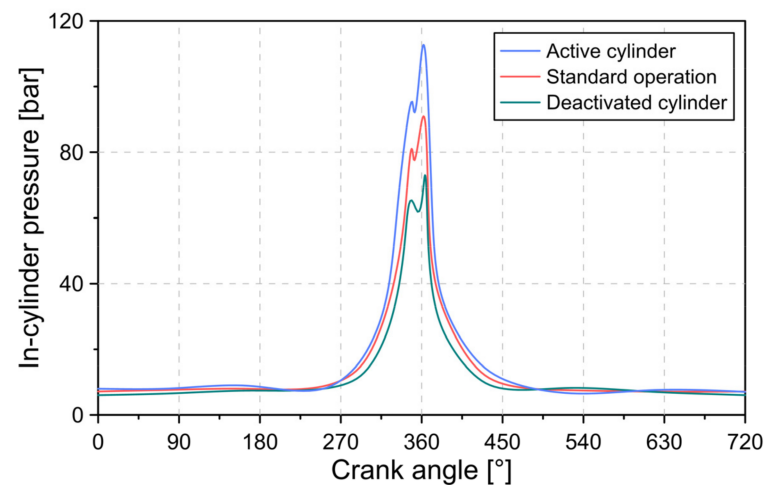

Figure 5. Combustion chamber pressure conditions for the active cylinder, cylinder in standard conditions, and cylinder deactivated.

The results of Figure 5 show that the minimum pressure in the combustion chamber occurs in the deactivated cylinder. This is a consequence of the closing of the intake valves and the exhaust valves on the deactivated cylinders. Therefore, only residual exhaust gas inside the cylinder is compressed and expanded. The opposite case occurs with the pressure in the active cylinders, which have the maximum combustion pressure. This pressure increase is necessary to maintain the same output power in relation to standard operating conditions. For the simulated conditions, a maximum combustion pressure of 111 bar, 89 bar, and 72 bar was obtained in the active cylinder, cylinder in standard conditions, and cylinder deactivated, respectively.

Figure 6 describes the cylinder wall temperature for the different conditions in the engine cylinders. The location of the liner wall used for the construction of the temperature curves is shown in Figure 7.

In general, the results of Figure 6 show that the interior of the active cylinder presents the highest temperature in the cylinder wall, which is maintained throughout the combustion cycle. On average, an average temperature of 179, 166, and 154 °C was observed in the active cylinder, cylinder in standard conditions, and cylinder deactivated, respectively. The results obtained are in agreement with what is reported in the literature [41]. The change in temperature has an effect on the physicochemical properties of the lubricating oil and, thus, on the minimum thickness of the lubrication film, as shown in Figure 8.
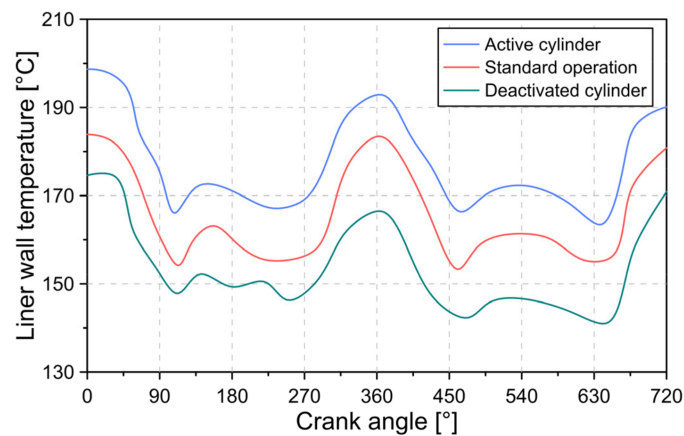
Figure 6. Cylinder wall temperature for the active cylinder, cylinder in standard conditions, and cylinder deactivated.
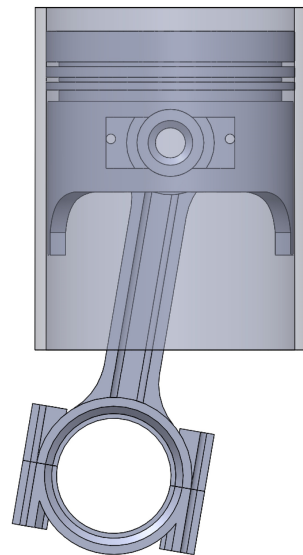

Figure 7. Cylinder liner wall location.

From the results described in Figure 8, it is evident that the condition of the active cylinder, cylinder in standard conditions, and cylinder deactivated have a significant influence on the minimum thickness of the lubrication film located between the cylinder liner and the piston rings. It was observed that the highest film thickness was located in the deactivated cylinder, which is directly associated with the lower pressure and temperature conditions of the lubricant. From the analysis of the thickness trend for the active cylinder, it is identified that the high temperature and the high load condition due to the increase in pressure lead to a drastic reduction in the thickness of the lubrication film. For the conditions tested, an increase of 23.80% and a reduction of 11.33% in the maximum thickness were obtained for the deactivated cylinder and the active cylinder compared to the standard conditions of the engine, respectively. The results obtained are in agreement with what is reported in the literature [41]. In general, the maximum thickness values were located in the middle position of the piston stroke. The greatest risk of cylinder liner wear occurs at the top dead center (TDC) and bottom dead center (BDC) of the engine.
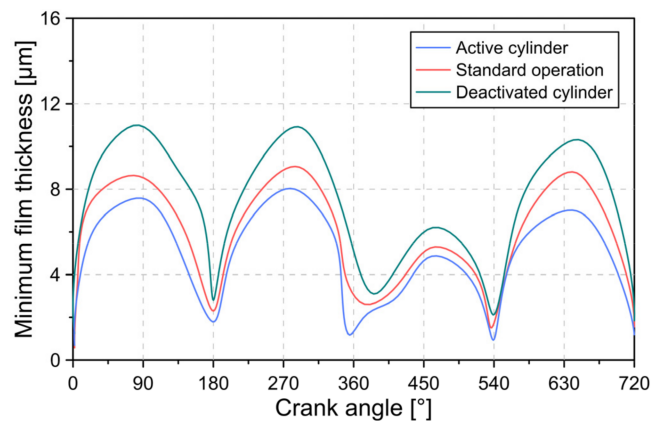
Figure 8. Minimum thickness of the lubrication film for the active cylinder, cylinder in standard conditions and cylinder deactivated in flooded lubrication.

5.2. Friction Force Analysis

Figure 9 shows the behavior of the hydrodynamic force for the active cylinder, cylinder in standard conditions, and cylinder deactivated.
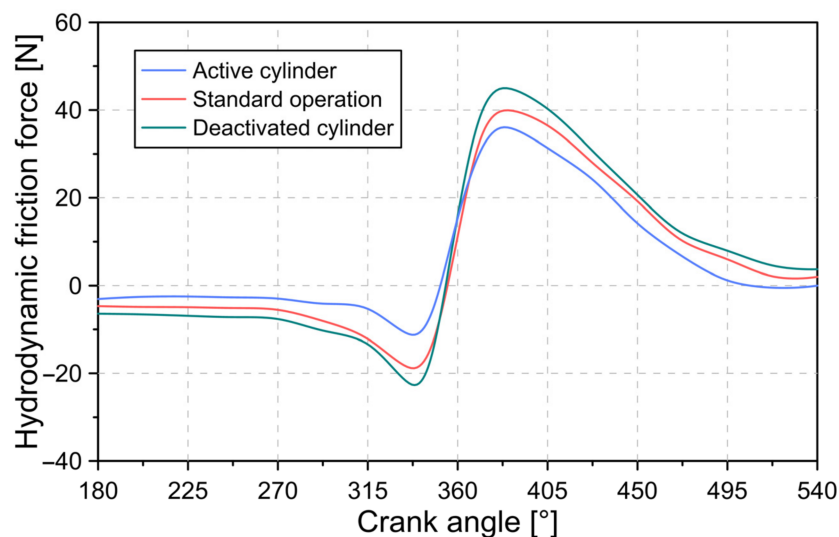

Figure 9. Hydrodynamic friction force for the active cylinder, cylinder in standard conditions, and cylinder deactivated in flooded lubrication.

The hydrodynamic force is directly related to the viscous forces of the lubricating oil. Compared to the cylinder in standard conditions, the high wall temperature in the active cylinder causes a reduction in the viscosity of the lubricating oil. Due to the above, a lower hydrodynamic friction force was obtained compared to the other conditions in the cylinders. The maximum hydrodynamic friction force recorded was 36.05, 39.85, and 45.01 N for the active cylinder, cylinder in standard conditions, and cylinder deactivated, respectively.

Asperity friction force trends for each cylinder are shown in Figure 10.
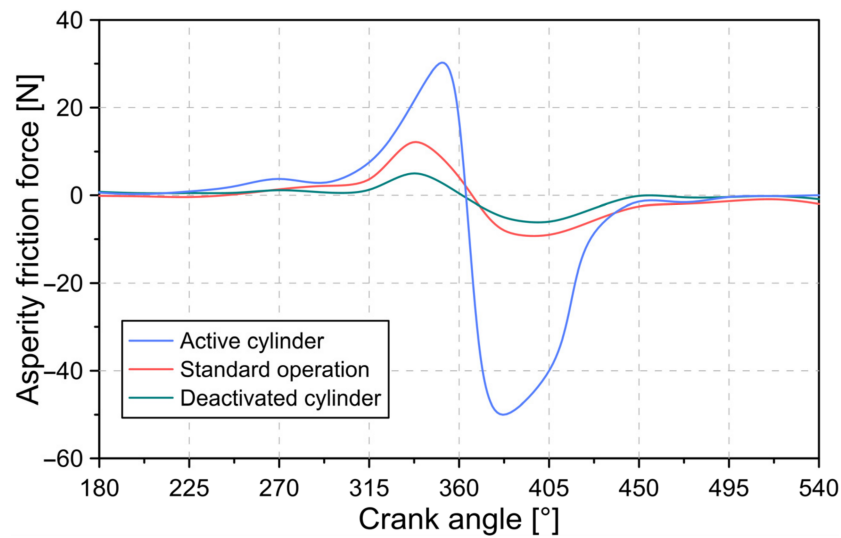
Figure 10. Asperity friction force for the active cylinder, cylinder in standard conditions, and cylinder deactivated in flooded lubrication.

Unlike the behavior described in Figure 9, the active cylinder presents a considerable increase in the friction force due to asperity in comparison with the cylinder in standard conditions and the cylinder deactivated. This result is a consequence of the greater thinning in the thickness of the lubrication film, as shown in Figure 8. This facilitates the contact between the rough surfaces of the piston rings and the cylinder liner. The greatest roughness friction force on the active cylinder occurs during the expansion stage of the engine.

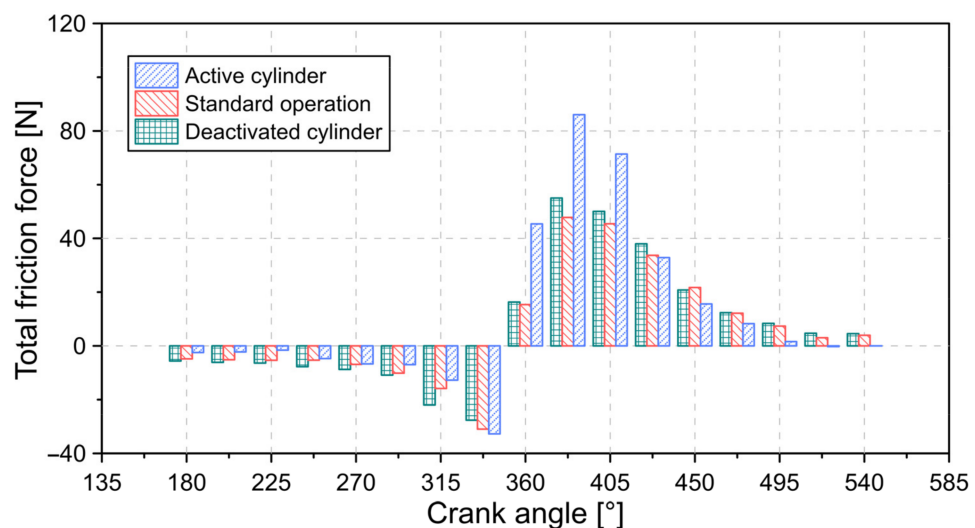The behavior of the total friction force throughout the combustion cycle is shown in Figure 11.

Figure 11. Total friction force for the active cylinder, cylinder in standard conditions, and cylinder deactivated in flooded lubrication.

In general, the deactivated cylinder exhibits a higher friction force compared to the cylinder in standard conditions. This behavior may be a consequence of the greater hydrodynamic friction force, as evidenced in Figure 9. During the intake and exhaust stages of the combustion cycle, it was observed that the minimum total friction force was present in the active cylinder. However, this behavior changed during the expansion stage as a result of the high asperity friction force in the active cylinder. The maximum total friction force recorded was 86.05, 47.85, and 55.01 N for the active cylinder, cylinder in

standard conditions, and cylinder deactivated, respectively. This has a direct impact on the power losses between the piston rings and the cylinder liner, as indicated in Figure 12.
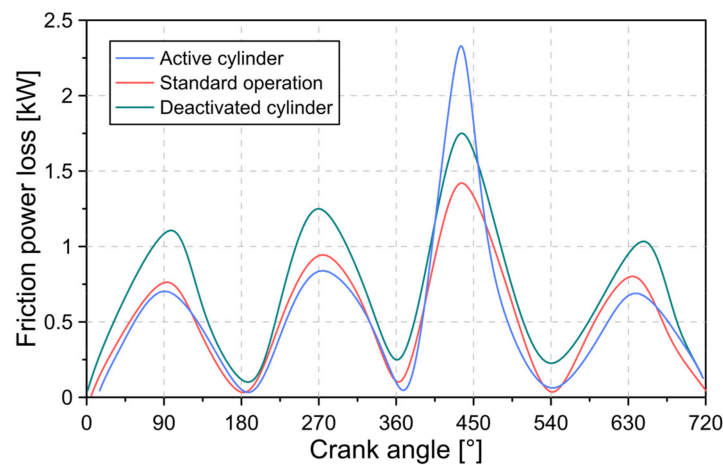

Figure 12. Loss power due to friction between the piston rings and the cylinder liner in flooded lubrication.

On average, the power loss due to friction was 0.51, 0.48, and 0.61 kW for the active cylinder, cylinder in standard conditions, and cylinder deactivated, respectively. The foregoing implies an increase in power loss by 63.90% and 23.17% for the active cylinder and deactivated cylinder compared to the standard conditions. Therefore, it is evident that the cylinder deactivation technology influences the tribological performance and the power loss by friction.

5.3. Blow-by Gas Analysis

Figure 13 illustrates the flow of gases into the crankcase throughout the combustion cycle for various in-cylinder conditions.
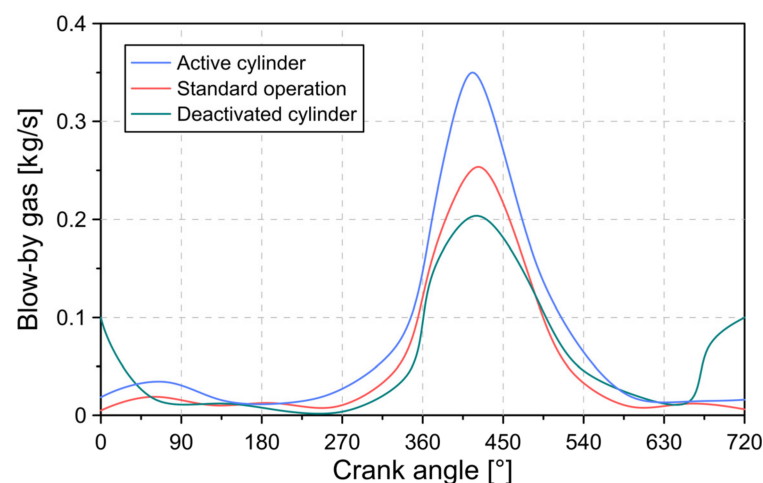

Figure 13. Blow-by gas for the active cylinder, cylinder in standard conditions, and cylinder deactivated.

In general, the greatest amount of combustion gas leakage occurs during the compression and expansion stages. However, in the case of the deactivated cylinders, additional leaks between the intake and exhaust stages were evidenced, which is due to the second compression of the combustion gases during the cycle by the closure of the intake and exhaust valves. The maximum recorded exhaust flow was 0.35, 0.25, and 0.20 kg/s for the active cylinder, standard condition cylinder, and deactivated cylinder, respectively. The greater number of leaks in the active cylinders is a consequence of the high pressure in the combustion chamber and the reduction in the thickness in the lubrication film.

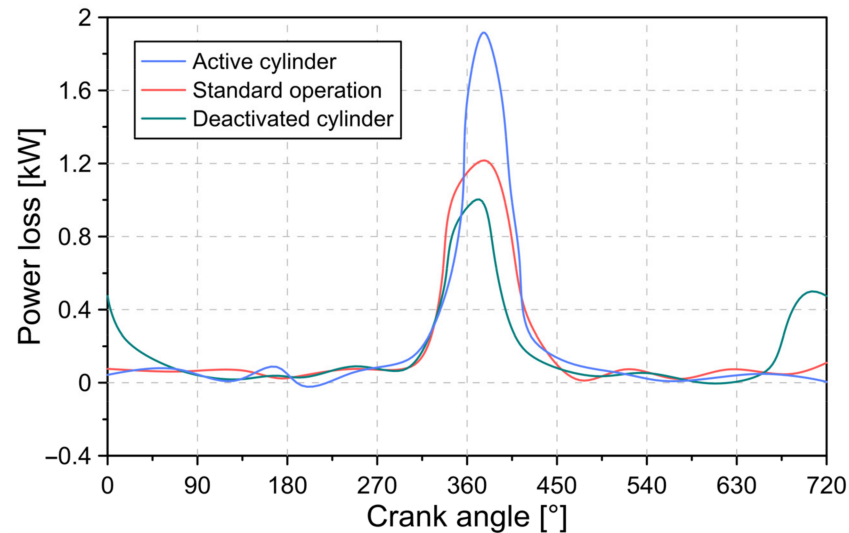The impact of blow-by gas on power loss is shown in Figure 14.

Figure 14. Loss power due to leakage of exhaust gases between the piston rings and the cylinder liner.

The results shown in Figure 14 describe a behavior similar to that observed in Figure 13. In general, the active cylinders cause an increase of 57.51% in the loss of power due to maximum leaks compared to the standard conditions. However, in the deactivated cylinders, a reduction of 17.60%, respectively, was obtained. This allows demonstrating that cylinder deactivation causes a significant increase in combustion cycle losses, which must be considered to evaluate the performance of internal combustion engines operating with cylinder deactivation technologies.

The effect of cylinder deactivation on emissions caused by combustion gases present in piston ring crevices is depicted in Figure 15.
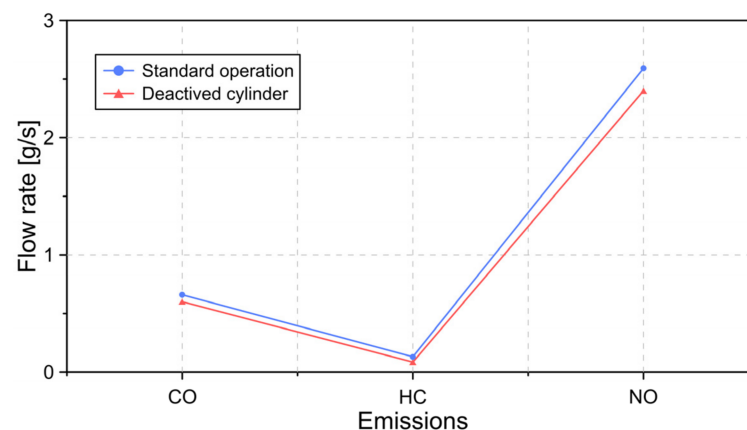

Figure 15. Polluting emissions in standard condition and cylinder deactivation.

From the results described in Figure 15, it is observed that the use of technologies such as cylinder deactivation allows reducing CO, HC, and NO emissions caused by combustion gases trapped in the crevices of the piston rings. This reduction implies less formation of unburned fuel inside the combustion chamber, which may be associated with the increase in the temperature of the cylinder wall. This behavior is in agreement with the results described in the literature [42]. Additionally, the increase in the temperature of the lubricating oil prevents its accumulation in the combustion chamber. This enables the oil evaporation rate to be reduced and, therefore, emissions. In general, a reduction of 9.09%, 8.26%, and 7.41% in CO, HC, and NO emissions, respectively, was evidenced.

6. Conclusions

In the present investigation, an analysis of the influence of technologies such as cylinder deactivation on the tribological characteristics and emission conditions in an internal combustion engine was carried out. For the development of the study, a tribological model was used, which was used to predict the characteristics of the lubrication film, friction conditions, blow-by gas, and deformation of the piston rings. To describe the movement of the piston inside the combustion chamber, a CFD model was built.

From the results, it was possible to demonstrate that the deactivation of cylinders has a high impact on the pressure and temperature conditions inside the combustion chamber. The active cylinders present an increase of 21.53% and 7.65% in the pressure and temperature in the cylinder wall. However, the deactivated cylinders produced a reduction of 19.24% and 7.07% in the previous parameters.

Cylinder deactivation influences the tribological performance between the piston rings and the cylinder liner. The active cylinders present a reduction of 11.33% in the minimum thickness of the lubrication film and an increase in the friction force due to the surface asperities between the piston rings and the cylinder liner. This implied a 33% increase in power losses due to friction.

Another disadvantage of the engine operating with deactivated cylinders is the increase in combustion gas leaks caused by the increase in pressure of the active cylinders and the closing of the intake and exhaust valves in the case of deactivated cylinders. In general, active cylinders show a 40% increase in combustion chamber leakage. However, the increase in cylinder wall temperature caused by cylinder deactivation allows the reduction of unburned fuel, which leads to a decrease of 9.09%, 8.26%, and 7.41% in CO, HC, and NO emissions.

Although the use of technologies such as cylinder deactivation allows significant fuel savings, it is necessary to consider the negative effects caused by this technology, such as the increase in combustion gas leaks and the increase in power loss by the highest frictional forces. This allows a more precise evaluation of the benefits of cylinder deactivation in internal combustion engines.

Abbreviations

The following abbreviations are used in this manuscript:

h	Thickness of the lubricant
P	Film pressure of the lubricating oil
v_p	Piston velocity
Z	Lubricant piezo-viscosity index
S_o	Thermo-viscosity index
α_o	Atmospheric piezo-viscosity coefficient
c_p, η_∞	Model constants
h_m	Minimum oil film thickness

h_p	Thickness of the oil due to the geometric profile of the piston ring
b	Piston ring axial width
f_v	Viscous friction force
A_e	Real area of contact area
A	Apparent contact area
$F_{2(\lambda)}$, $F_{5/2(\lambda)}$	Statistical function
f_a	Asperity friction force
E_{ss}	Limiting Eyring shear stress
W_a	Asperity contact load
E'	Equivalent Young's modulus of elasticity
E_c	Modulus of elasticity of the cylinder liner
E_p	Modulus of elasticity of the piston ring
v_c	Poisson's ratio of the cylinder liner
v_p	Poisson's ratio of the piston ring
$\dot{m}_f$	Mass flow
C_d	Coefficient of discharge
T_u	Orifice upstream temperature
R	Gas constant
A_g	Ring end-gap area
f_m	Compressibility factor
p_d	Downstream pressure
p_u	Upstream pressure
I_p	Second area moment of inertia
R_p	Ring radius of curvature
f_r	Radial force acting on the piston ring
f_t	Tangential force acting on the piston ring
Greek Letters	
η	Viscosity of the lubricant
ρ	Density of the lubricating oil
β	Coefficient of thermal expansion
β_o	Thermo-viscosity coefficient
δ_o	Crown height
ϕ_x, ϕ_y	Pressure flow factors
σ	Composite roughness
ϕ_c	Contact factor
ϕ_s	Shear flow factor
τ_{ss}	Viscous shear stress
ξ	Asperity distribution per unit contact area
κ	Average asperity tip radius of curvature
λ	Stribeck lubricant film ratio
ζ	Coefficient of asperity shear strength
ρ_p	Piston ring material density
A_p	Cross-sectional area of the ring
θ	Angular position along the ring circumference

References

1. Gurt, A.; Khonsari, M. The use of entropy in modeling the mechanical degradation of grease. *Lubricants* **2019**, *7*, 82. [CrossRef]
2. Chong, W.W.F.; Hamdan, S.H.; Wong, K.J.; Yusup, S. Modelling Transitions in Regimes of Lubrication for Rough Surface Contact. *Lubricants* **2019**, *7*, 77. [CrossRef]
3. Ochoa, G.V.; Prada, G.; Duarte-Forero, J. Carbon footprint analysis and advanced exergo-environmental modeling of a waste heat recovery system based on a recuperative organic Rankine cycle. *J. Clean. Prod.* **2020**, *274*, 122838–122857. [CrossRef]
4. Leach, F.; Kalghatgi, G.; Stone, R.; Miles, P. The scope for improving the efficiency and environmental impact of internal combustion engines. *Transp. Eng.* **2020**, *1*, 100005. [CrossRef]
5. Richardson, D.E. Review of Power Cylinder Friction for Diesel Engines. *J. Eng. Gas Turbines Power* **2000**, *122*, 506–519. [CrossRef]
6. Valencia, G.; Fontalvo, A.; Duarte Forero, J. Optimization of waste heat recovery in internal combustion engine using a dual-loop organic Rankine cycle: Thermo-economic and environmental footprint analysis. *Appl. Therm. Eng.* **2021**, *182*, 116109. [CrossRef]
7. Morris, N.; Mohammadpour, M.; Rahmani, R.; Rahnejat, H. Optimisation of the piston compression ring for improved energy efficiency of high performance race engines. *Proc. Inst. Mech. Eng. Part D J. Automob. Eng.* **2017**, *231*, 1806–1817. [CrossRef]

8. Oglieve, C.J.; Mohammadpour, M.; Rahnejat, H. Optimisation of the vehicle transmission and the gear-shifting strategy for the minimum fuel consumption and the minimum nitrogen oxide emissions. *Proc. Inst. Mech. Eng. Part D J. Automob. Eng.* **2017**, *231*, 883–899. [CrossRef]

9. Fitzsimons, B. Introduction to the importance of fuel efficiency and role of the Encyclopedic research project. In Proceedings of the IMechE Seminar: A Drive for Fuel Efficiency, Loughborough, UK, 21 September 2011.

10. Forero, J.D.; Ochoa, G.V.; Alvarado, W.P. Study of the Piston Secondary Movement on the Tribological Performance of a Single Cylinder Low-Displacement Diesel Engine. *Lubricants* **2020**, *8*, 97. [CrossRef]

11. Menzel, G.; Och, S.H.; Mariani, V.C.; Moura, L.M.; Domingues, E. Multi-objective optimization of the volumetric and thermal efficiencies applied to a multi-cylinder internal combustion engine. *Energy Convers. Manag.* **2020**, *216*, 112930. [CrossRef]

12. Balakheli, M.M.; Chahartaghi, M.; Sheykhi, M.; Hashemian, S.M.; Rafiee, N. Analysis of different arrangements of combined cooling, heating and power systems with internal combustion engine from energy, economic and environmental viewpoints. *Energy Convers. Manag.* **2020**, *203*, 112253. [CrossRef]

13. Cao, J.; Jia, M.; Niu, B.; Chang, Y.; Xu, Z.; Liu, H. Establishment of an improved heat transfer model based on an enhanced thermal wall function for internal combustion engines operated under different combustion modes. *Energy Convers. Manag.* **2019**, *195*, 748–759. [CrossRef]

14. Agarwal, A.K.; Mustafi, N.N. Real-world automotive emissions: Monitoring methodologies, and control measures. *Renew. Sustain. Energy Rev.* **2021**, *137*, 110624. [CrossRef]

15. Tornatore, C.; Bozza, F.; De Bellis, V.; Teodosio, L.; Valentino, G.; Marchitto, L. Experimental and numerical study on the influence of cooled EGR on knock tendency, performance and emissions of a downsized spark-ignition engine. *Energy* **2019**, *172*, 968–976. [CrossRef]

16. Dong, H.; Zhao, Z.; Fu, J.; Liu, J.; Li, J.; Liang, K.; Zhou, Q. Experiment and simulation investigation on energy management of a gasoline vehicle and hybrid turbocharger optimization based on equivalent consumption minimization strategy. *Energy Convers. Manag.* **2020**, *226*, 113518. [CrossRef]

17. Nazoktabar, M.; Jazayeri, S.A.; Parsa, M.; Ganji, D.D.; Arshtabar, K. Controlling the optimal combustion phasing in an HCCI engine based on load demand and minimum emissions. *Energy* **2019**, *182*, 82–92. [CrossRef]

18. Yusri, I.M.; Mamat, R.; Najafi, G.; Razman, A.; Awad, O.I.; Azmi, W.H.; Ishak, W.F.W.; Shaiful, A.I.M. Alcohol based automotive fuels from first four alcohol family in compression and spark ignition engine: A review on engine performance and exhaust emissions. *Renew. Sustain. Energy Rev.* **2017**, *77*, 169–181. [CrossRef]

19. García, A.; Monsalve-Serrano, J.; Martínez-Boggio, S.; Wittek, K. Potential of hybrid powertrains in a variable compression ratio downsized turbocharged VVA Spark Ignition engine. *Energy* **2020**, *195*, 117039. [CrossRef]

20. Wittek, K.; Geiger, F.; Vaz, M.G.J. Characterization of the system behaviour of a variable compression ratio (VCR) connecting rod with eccentrically piston pin suspension and hydraulic moment support. *Energy Convers. Manag.* **2020**, *213*, 112814. [CrossRef]

21. López, J.J.; Garcia, A.; Monsalve-Serrano, J.; Cogo, V.; Wittek, K. Potential of a two-stage variable compression ratio downsized spark ignition engine for passenger cars under different driving conditions. *Energy Convers. Manag.* **2020**, *203*, 112251. [CrossRef]

22. Muhamad Said, M.F.; Latiff, Z.A.; Zainal Abidin, S.F.; Zahari, I. Investigation of Intake Valve Strategy on the Cylinder Deactivation Engine. In *Applied Mechanics and Materials*; Trans Tech Publications Ltd.: Bäch, Switzerland, 2016; Volume 819, pp. 459–465.

23. Zhao, J.; Xi, Q.; Wang, S.; Wang, S. Improving the partial-load fuel economy of 4-cylinder SI engines by combining variable valve timing and cylinder-deactivation through double intake manifolds. *Appl. Therm. Eng.* **2018**, *141*, 245–256. [CrossRef]

24. Singh, D.; Gu, F.; Fieldhouse, J.D.; Singh, N.; Singal, S.K. Prediction and analysis of engine friction power of a diesel engine influenced by engine speed, load, and lubricant viscosity. *Adv. Tribol.* **2014**, *2014*, 928015. [CrossRef]

25. Bewsher, S.R.; Turnbull, R.; Mohammadpour, M.; Rahmani, R.; Rahnejat, H.; Offner, G.; Knaus, O. Effect of cylinder de-activation on the tribological performance of compression ring conjunction. *Proc. Inst. Mech. Eng. Part J J. Eng. Tribol.* **2017**, *231*, 997–1006. [CrossRef]

26. Tian, T. Dynamic behaviours of piston rings and their practical impact. Part 2: Oil transport, friction and wear of ring/liner interface and the effects of piston and ring dynamics. *Proc. Inst. Mech. Eng. Part J J. Eng. Tribol.* **2002**, *216*, 229–248. [CrossRef]

27. Guo, Y.; Lu, X.; Li, W.; He, T.; Zou, D. A mixed-lubrication model considering elastoplastic contact for a piston ring and application to a ring pack. *Proc. Inst. Mech. Eng. Part D J. Automob. Eng.* **2015**, *229*, 174–188. [CrossRef]

28. Patir, N.; Cheng, H.S. An Average Flow Model for Determining Effects of Three-Dimensional Roughness on Partial Hydrodynamic Lubrication. *J. Lubr. Technol.* **1978**, *100*, 12–17. [CrossRef]

29. Dowson, D.; Higginson, G.R. A Numerical Solution to the Elasto-Hydrodynamic Problem. *J. Mech. Eng. Sci.* **1959**, *1*, 6–15. [CrossRef]

30. Houpert, L. New Results of Traction Force Calculations in Elastohydrodynamic Contacts. *J. Tribol.* **1985**, *107*, 241–245. [CrossRef]

31. Gu, C.; Meng, X.; Xie, Y.; Kong, X. Performance of surface texturing during start-up under starved and mixed lubrication. *J. Tribol.* **2017**, *139*, 11702. [CrossRef]

32. Rahmani, R.; Theodossiades, S.; Rahnejat, H.; Fitzsimons, B. Transient elastohydrodynamic lubrication of rough new or worn piston compression ring conjunction with an out-of-round cylinder bore. *Proc. Inst. Mech. Eng. Part J J. Eng. Tribol.* **2012**, *226*, 284–305. [CrossRef]

33. Teodorescu, M.; Balakrishnan, S.; Rahnejat, H. Integrated Tribological Analysis within a Multi-physics Approach to System Dynamics. In *Tribology and Interface Engineering Series*; Elsevier: Amsterdam, The Netherlands, 2005; Volume 48, pp. 725–737.

34. Greenwood, J.A.; Tripp, J.H. The Contact of Two Nominally Flat Rough Surfaces. *Proc. Inst. Mech. Eng.* **1970**, *185*, 625–633. [CrossRef]

35. Turnbull, R.; Dolatabadi, N.; Rahmani, R.; Rahnejat, H. An assessment of gas power leakage and frictional losses from the top compression ring of internal combustion engines. *Tribol. Int.* **2020**, *142*, 105991–106002. [CrossRef]

36. Theaker, M.; Rahmani, R.; Rahnejat, H. Prediction of Ring-Bore Conformance and Contact Condition and Experimental Validation. In Proceedings of the ASME 2012 Internal Combustion Engine Division Spring Technical Conference, Torino, Italy, 6–9 May 2012; pp. 885–892.

37. Popoola, O.; Cao, Y. The influence of turbulence models on the accuracy of CFD analysis of a reciprocating mechanism driven heat loop. *Case Stud. Therm. Eng.* **2016**, *8*, 277–290. [CrossRef]

38. Zavos, A.; Nikolakopoulos, P.G. Tribology of new thin compression ring of fired engine under controlled conditions-A combined experimental and numerical study. *Tribol. Int.* **2018**, *128*, 214–230. [CrossRef]

39. Tsujiuchi, N.; Koizumi, T.; Hamada, K.; Okamura, M.; Tsukijima, H. Optimization of profile for reduction of piston slap excitation. In *SAE Technical Papers*; SAE: Warrendale, PA, USA, 2004.

40. Gore, M.; Theaker, M.; Howell-Smith, S.; Rahnejat, H.; King, P.D. Direct measurement of piston friction of internal-combustion engines using the floating-liner principle. *Proc. Inst. Mech. Eng. Part D J. Automob. Eng.* **2014**, *228*, 344–354. [CrossRef]

41. Morris, N.; Mohammadpour, M.; Rahmani, R.; Johns-Rahnejat, P.M.; Rahnejat, H.; Dowson, D. Effect of cylinder deactivation on tribological performance of piston compression ring and connecting rod bearing. *Tribol. Int.* **2018**, *120*, 243–254. [CrossRef]

42. Wang, X.; Stone, C.R. A study of combustion, instantaneous heat transfer, and emissions in a spark ignition engine during warm-up. *Proc. Inst. Mech. Eng. Part D J. Automob. Eng.* **2008**, *222*, 607–618. [CrossRef]